A 22-m Operation Range Semi-Passive UHF RFID Sensor Tag With Flexible Thermoelectric Energy Harvester

Hector Solar, Andoni Beriain, *Member, IEEE*, Ainhoa Rezola, David del Rio, *Member, IEEE*, and Roc Berenguer, *Senior Member, IEEE*

***Abstract*—This article presents a wireless temperature sensor tag able to work in both fully passive mode and in semi-passive mode when assisted by a flexible thermoelectric generator (TEG). The sensor tag consists of an EPC C1G2/ISO 18000-6C ultrahigh-frequency (UHF) radio frequency identification (RFID) integrated circuit (IC) connected to a low-power microcontroller unit (MCU) that samples and collects the temperature from a digital temperature sensor. With a temperature gradient as low as 2.5 °C, the test results show that the TEG provides an output power of 400 μW with an output voltage of 40 mV. By means of an up-converter in order to boost the TEG output voltage, this harvester supplies the power required to the sensor tag for a 2-conv/s data rate in semi-passive mode. Moreover, when the tag operates in semi-passive mode, a communication range of 22.2 m is measured for a 2-W effective radiated power (ERP) reader. To the best of our knowledge, the proposed TEG-assisted sensor tag shows the longest communication range and the only one that provides stable external power at low-temperature gradients. The measured performance and the chosen architecture allow using the wireless sensor in multiple industrial or biomedical applications.**

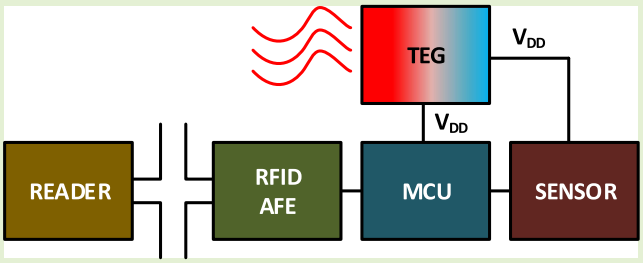

***Index Terms*— Energy harvesting, integrated circuit (IC), Internet of Things (IoT), radio frequency identification (RFID), thermoelectric generator (TEG).**

I. Introduction

THE projections for the market of the Internet of Things (IoT) foresee billions of IoT devices deployed across multiple industrial applications [1]. Such a massive number of IoT devices demands technologies that allow for low-cost wireless sensing solutions with high autonomy and low maintenance devices. Active wireless sensors using communication protocols such as Zigbee or Bluetooth low energy (BLE) typically require a continuous power supply, usually from a battery, to work properly. The advantage of these devices is that their communication range is in the order of tens to hundreds of meters. However, it comes at a price: greater size, weight, or cost. In addition, these sensors require maintenance in order to recharge or replace the battery. Therefore, there is a strong interest to provide battery-free solutions with no maintenance requirements and with communication ranges of tens of meters.

Among the different alternatives, the ultrahigh-frequency (UHF) RFID technology has become a highly popular IoT solution for a wide range of industry segments [2], [3], [4]. This technology initially started as wireless object tracking and identification solution. However, in the recent years, it is possible to find many reference designs that combine the UHF RFID technology with sensor capabilities providing low cost and high autonomy wireless sensors for a wide range of fields, such as healthcare, transport, or industry, among others [1], [9], [10], [11], [12], [13], [14], [15], [16], [17], [18], [19], [20], [21], [22], [23], [24], [25], [26], [27], [28], [29], [30], [31], [32], [33], [34], [35], [36].

In spite of the popularity of the UHF RFID technology, the drawback of the limited system communication range still exists. A number of alternatives can be found in the prior art in order to overcome this problem, such as harmonic

Manuscript received 5 August 2022; accepted 17 August 2022. Date of publication 5 September 2022; date of current version 14 October 2022. This work was supported by the project MOONLIGHT of the Spanish Ministry of Science and Innovation under Grant PID2020-117251RB-C22. The associate editor coordinating the review of this article and approving it for publication was Dr. Wei Tang. *(Corresponding author: Hector Solar.)*

Hector Solar, Andoni Beriain, Ainhoa Rezola, and Roc Berenguer are with the Department of Electrical and Electronic Engineering, Tecnun-School of Engineering University of Navarra, Donostia-San Sebastian, 20018 Gipuzkoa, Spain (e-mail: hsolar@tecnun.es; aberain@tecnun.es; argarciandia@tecnun.es; rberenguer@tecnun.es).

David del Rio is with the Information and Communications Technologies Division, CEIT BRTA, Donostia-San Sebastian, 20018 Gipuzkoa, Spain (e-mail: ddelrio@ceit.es).

Digital Object Identifier 10.1109/JSEN.2022.3202634

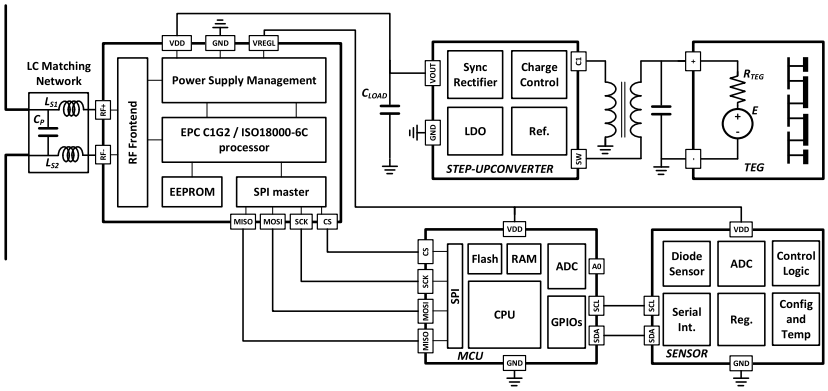

Fig. 1. Block diagram of the sensor tag connected to the energy harvester module.

energy harvesting, repeaters, multiantenna readers, multistatic scatter techniques, and alternative energy sources [5], [6], [7], [8]. Specifically, this work focuses on an EPC C1G2 compliant batteryless sensor tag semi-passive solution assisted by a thermoelectric generator (TEG).

In fact, based on the energy harvesting sources, RFID tags can be classified as active, passive, or semi-passive. Active tags are battery-powered with the advantage of long reading ranges but show greater size, weight, or cost and the need for maintenance for battery replacement.

The fully passive RFID sensor technology harvests the energy for its own operation from the energy of the RF waveform transmitted by the reader, whereas the communication with the reader is performed by backscatter modulation of the RF waveform. As the battery is avoided, passive tags show unlimited lifetime and low size, weight, or cost. However, fully passive RFID sensor tags suffer from a short communication range due to the need of powering both the sensing process and the RF communications. Many efforts have been done in order to add sensing capabilities to passive UHF RFID tags without excessively degrading the communication range [9], [10], [11], [12], [13], [14], [15], [16], [17], [18], [19], [20], [21]. However, even though the RFID IC of these tags is EPC C1G2 compliant, they have the issue of being custom solutions with limited capability to accept new sensors, low data accuracy or resolution, and a range of only several meters.

As an alternative, a number of solutions are found in the recent literature using semi-passive sensor tags for range extension [1], [22], [23], [24], [25], [26], [27], [28], [29], [30], [31], [32], [33], [34], [35], [36], where only half of them implement energy harvesting modules instead of batteries [22], [23], [24], [25], [26], [27], [28], [29]. Among them, only one of them discusses a TEG as an energy harvester, with limited power harvesting and read range [28]. In fact, the predominant energy harvester for semi-passive RFID applications seems to be the use of photovoltaic (PV) modules. One reason is that PV provides lower prices per area when compared to TEG-based solutions [37], [38]. In addition, PV modules show in general better performance with respect to power densities and higher efficiency than TEGs. This is true when referring to PV outdoor applications, although the gap is reduced when dealing with PV indoor solutions [39], [40]. Nevertheless, even though the implementation of TEGs as energy harvesters poses more design challenges, their use combined with the semi-passive RFID technology has a great potential in multiple applications in which thermal energy is present and/or solar energy is not ensured. The biomedical field where the human body is considered a near-continuous source of thermal energy is the first example. In addition, heat sources can also be found in many other sectors, such as the steel, oil, chemical, or energy generation industries [41], [42], [43]. Moreover, flexible TEGs are of special interest as they can be adapted to the shape of the energy source.

Given the limited solutions offered in the literature and their application potential, a wireless UHF sensor tag assisted by a flexible TEG is presented. In addition, the tag comprises the UHF RFID IC following the EPC C1G2/ISO 18000-6C communication standard, a TEG with the necessary power boost converter, a microprocessor, and a digital temperature sensor connected to it by means of a standard interintegrated circuit (I2C) protocol. The tag performance in both passive and semi-passive modes has been tested.

This article is organized as follows. Section II conducts an overview of the proposed wireless temperature sensor. Section III presents a detailed analysis of the system energy requirement. Section IV presents the measurements of the individual parts of the wireless sensor, such as the TEG or the RFID, as well as the overall performance of the complete sensor. Finally, Section V concludes this article.

II. Tag Description

Fig. 1 shows the block diagram of the semi-passive tag. As it is shown, it comprises an EPC C1G2/ISO 18000-6C compliant tag IC connected to a 2-dBi dipole antenna [44]. In addition, a differential *LC* network provides conjugate matching between the antenna and the input impedance of the tag IC in passive mode. In contrast, the IC sensitivity depends on the mode and the expected load. In the passive mode, it claims -14 dBm for pure identification and -10 dBm when supplying external sensors. In the semi-passive mode, it improves down to -24 dBm. In order to work in the semi-passive mode, an external supply voltage between 1.4 and 3 V must be supplied. It must also be noted that the chip's input impedance changes when it shifts from the passive to the semi-passive modes from $80-493j$ to $35-451j$ at 868 MHz [44]. As it will be discussed, this fact must be considered in order

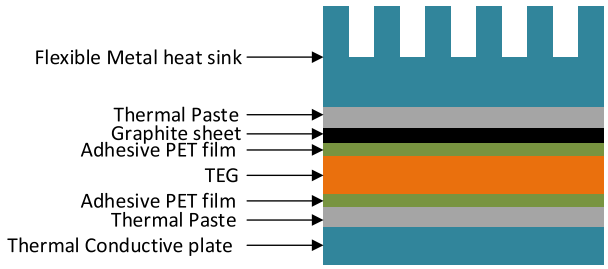

Fig. 2. Cross section view of layers of the TEG module.

to choose the best impedance matching between the chip and the antenna. Finally, the IC adds a configurable LDO regulator between 1.2 and 3 V for regulated power supply generation. This LDO is used to supply the microcontroller unit (MCU) and the digital temperature sensor.

In contrast, the RFID IC controls an MSP430 low-power MCU via its built-in serial peripheral interface (SPI) master module. The MCU in turn reads a digital temperature sensor using the I2C protocol [45]. It corresponds to a low-power sensor that shows 1 °C accuracy from −40 °C to 125 °C temperature range. In addition, this sensor may work in continuous conversion mode, with a programmable conversion rate (0.25, 1, 4, or 8 conv/s) so that a compromise between energy consumption and time resolution can be reached. Even though a temperature sensor has been chosen for the prototype, as long as an MCU is incorporated into the tag, the temperature sensor could be substituted by any other low-power digital or even an analog sensor, using the MCU internal analog-to-digital converter (ADC).

The tag is completed with the TEG module and the energy conditioning circuitry, which are described and characterized in detail in Section III. The chosen TEG has an 85 mm × 64 mm area and comprises 170 thermocouples of p- and n-type pair legs embedded in a flexible proprietary polymer material [46], [47]. It also mounts a 15-mm height flexible heat sink [48]. This flexible heat sink allows one degree of freedom for TEG bending. The cross section view of the layers required for optimal temperature transfer is shown in Fig. 2. As seen, a graphite sheet is placed between the TEG and the heat sink as it improves the lateral thermal conductivity. In addition, the polyethylene terephthalate (PET) films allow for electrical insulation between the TEG and the electrically conductive bottom plate or the heat sink. It is also required a thermal paste with high thermal conductivity, 8.5 W/mK in this case [49]. Finally, for test purposes, the thermal conductive bottom plate is a planar copper layer.

Regarding the power conditioning electronics, given that the output voltage of the TEG is too low for directly powering the tag, a step-up converter is required. The LTC3108 step-up converter has been chosen for several reasons [50]. First, this up-converter may operate from input voltages as low as 20 mV and this ensures voltage up-conversion even for very low-temperature gradients between the TEG's cold and hot sides. Second, its output voltage can be programed for different output voltage levels from 2.35 to 5 V, being 2.35 V the chosen level for this design. The last reason is that its input resistance, around 3.5 Ω, greatly coincides with the output impedance of the TEG (2.95 Ω) for maximum power transfer [46]. This is

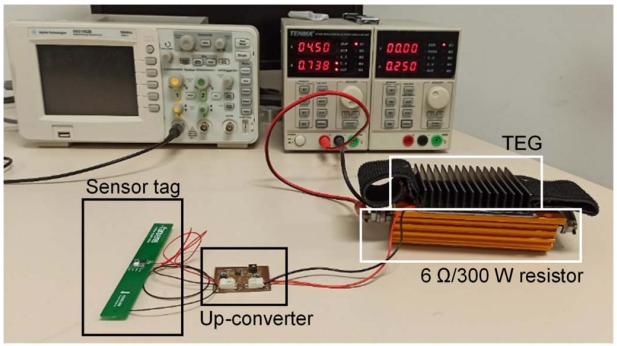

Fig. 3. Photograph of the tag prototype.

crucial for maximizing the power efficiency of the voltage conversion. Finally, as observed in Fig. 1, a storage capacitor of 220 μF is included at the output of the step-up converter in order to absorb the dynamic current consumption of the system. A photograph of the complete prototype is shown in Fig. 3.

III. Analysis and Characterization of the Thermoelectric Module

This section discusses the power consumption requirements of the sensor tag and characterizes both the TEG module alone and when connected with the step-up converter in terms of its power generation capabilities.

A. Power Budget Analysis

In order to ensure that the TEG energy generation is enough for the tag energy requirements, a power budget analysis is required. As aforementioned, the semi-passive RFID sensor tag comprises the RFID IC, the low-power microcontroller, and the digital temperature sensor. The average power consumption of the tag is as follows: the RFIC IC consumes 7 μA when it is active. For a temperature resolution of 2 samples/s, the microcontroller wakes up from LPM3 sleep mode every 500 ms, and, when active, it consumes 1 mA for 1 ms. As long as the microcontroller requires a minimum of 1.8 V, both the MCU and the temperature sensor are supplied with the regulated output from the RFID IC configured at 2 V. An external supply to the IC of 2.35 V is then chosen among the selectable values of the step-up converter [50]. As mentioned before, the temperature sensor can be configured to get temperature samples autonomously. As a 2-conv/s rate is not available, the chosen temperature conversion rate is 4 conv/s in this case, with an active current consumption of 40-μA and 25-ms acquisition time per conversion. Considering the active current consumption and active time along with the standby current, the average current consumption of the temperature sensor is 6 μA, whereas it is 3 μA for the MCU. The average power consumption required for the overall sensor tag is 34.5 μW for a sensor data communication rate of 2 temperature samples/s, as shown in Fig. 4.

Regarding the TEG power generation capabilities, its equivalent ac electrical resistances at 27 °C are RTEG = 2.95 Ω, while the p- and n-type pairs (p-type: $Bi_{0.3}Sb_{1.7}Te_3$, n-type: $Bi_2Se_{0.3}Te_{2.7}$) have a Seebeck coefficient of $\alpha_p = 176\ \mu VK^{-1}$

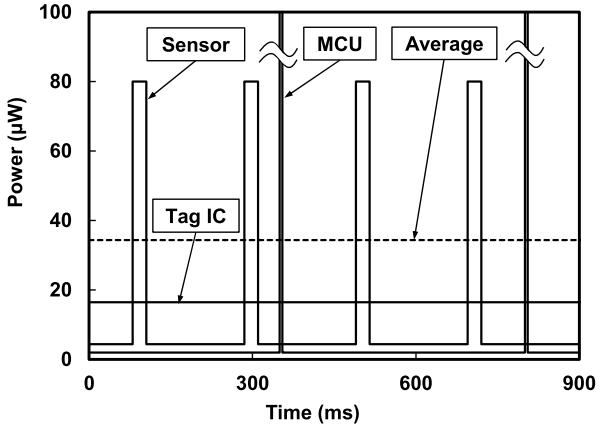

Fig. 4. Current consumption profile of the sensor, MCU and tag IC, and average current consumption.

TABLE I
AVAILABLE OUTPUT VOLTAGE AND POWER AT THE TEG OUTPUT

ΔT (°C)	V_{OC} (mV)	V_L (mV)	P_{LMAX} (µW)	P_{OUT_CONV} (µW)	P_{OUT_LDO} (µW)
1.0	57.3	28.6	278	97	83
1.3	74.5	37.2	470	165	140
1.5	85.9	43.0	626	219	186
1.8	103.1	51.6	901	315	268
2.0	114.6	57.3	1113	390	331

and $\alpha_n = -161\ \mu\text{VK}^{-1}$, respectively [46]. With these values, it is first possible to calculate the open-circuit voltage between terminals by means of the following equation:

$$V_{\text{OC}} = N\alpha_{pn}\Delta T \tag{1}$$

being ΔT the temperature difference across the thermocouples, N the total number of thermocouples, and α_{pn} the thermocouple's Seebeck coefficient

$$\alpha_{pn} = \alpha_{p-}\alpha_n. \tag{2}$$

For maximum power transfer, i.e., with a load equal to the internal TEG resistance, the output voltage is halved (3) and the maximum output power is obtained from the following equation:

$$V_L = V_{\text{OC}}\frac{R_L}{(R_L + R_{\text{TEG}})} \tag{3}$$

$$P_{L,\text{MAX}} = \frac{V_{\text{OC}}^2}{4R_L}. \tag{4}$$

Knowing that the TEG module comprises 170 p-type/n-type pair legs, several theoretical values for the output power and output voltage levels are shown in Table I from 1 °C to 2 °C temperature gradients. As shown, the available output power is more than enough to supply the tag in semi-passive mode even for low-temperature gradients. Still, given the low TEG's output voltage levels the effect of the step-up converter must also be considered. As mentioned before, the step-up converter is able to up-convert small input voltage levels, down to 20 mV. This is achieved by means of a 1:100 turn ratio transformer at the input of the converter. Thus, the converter should be able to provide 2.35 V to the tag even for 1 °C of a temperature gradient. In addition, the converter's input resistance is 3.5 Ω for a 50-mV input voltage. This resistance value is higher but close to the internal 2.95-Ω output resistance of the TEG, so that power transfer should be close to its maximum. Moreover, the optimal loads for TEGs tend to be higher than their internal resistance, given their nonlinear behavior [46]. Therefore, maximum power transfer is expected and, hence, an optimal conversion efficiency in the converter [50]. It can be concluded that, in theory, the TEG module connected to the converter will be able to offer enough power to the semi-passive tag with a proper output voltage level.

Still, the efficiency of the tag is limited so it needs to be included in the calculations. In addition, for the case of the MCU and the temperature sensor that are supplied by the LDO, the efficiency of the LDO must be also considered. Therefore, the power at the output of the step-up converter and the LDO is given in the following equations:

$$P_{\text{OUT\_CONV}} = P_{L\_\text{MAX}} \cdot \eta_{\text{CONV}} \tag{5}$$

$$P_{\text{OUT\_LDO}} = P_{L\_\text{MAX}} \cdot \eta_{\text{CONV}} \cdot \eta_{\text{LDO}} \tag{6}$$

where η_{CONV} and η_{LDO} are the efficiencies in % of the step-up converter and the LDO, respectively, and are calculated by the following equations:

$$\eta_{\text{CONV}} = 100 \times \frac{P_{\text{OUT}}}{P_{\text{IN}}} \tag{7}$$

$$\eta_{\text{LDO}} = 100 \times \frac{I_0 V_0}{(I_0 + I_q)\, V_I} \tag{8}$$

where I_O and I_q are the output and quiescent currents, respectively, and V_O and V_I are the output and input voltages, respectively. As shown in Table I, the input voltage of the step-up converter (VL) ranges from 28.6 to 57.3 mV. This corresponds to a minimum efficiency of 35% for the converter [50]. In addition, the I_q of the tag's LDO is 220 nA, which results in 85% efficiency of the tag's LDO when supplying the 9 μA required for both the MCU and the temperature sensor [44]. These values allow calculating the power at the output of the step-up converter or the step-up converter plus the LDO shown in Table I.

B. TEG Module Characterization

In order to confirm this last assumption, the TEG module has been first characterized using a 6-Ω/300-W resistor. As shown in Fig. 3, this resistor has been used as a heat source for which the temperature can be chosen by modifying the current that flows through it by means of a dc voltage source. The TEG module temperature gradient has been measured by means of a thermistor placed at the 6-Ω resistor planar face as the hot side and among the rack of the heat sink as the cold side. The ambient temperature is 23 °C, whereas the temperature for the heat source is set to 36.8 °C. This last value emulates the body temperature in healthcare applications and it is considered a worst case scenario as, for example, much higher temperature can be found in industrial applications [42]. The TEG module has been placed both in horizontal and

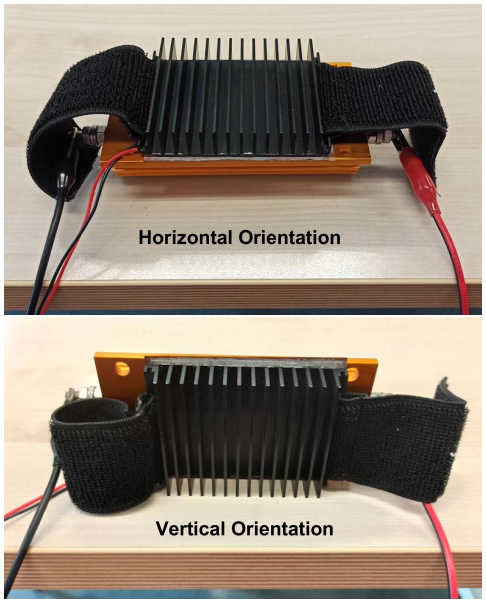

Fig. 5. Photographs of the horizontal and vertical orientations for the TEG module characterization.

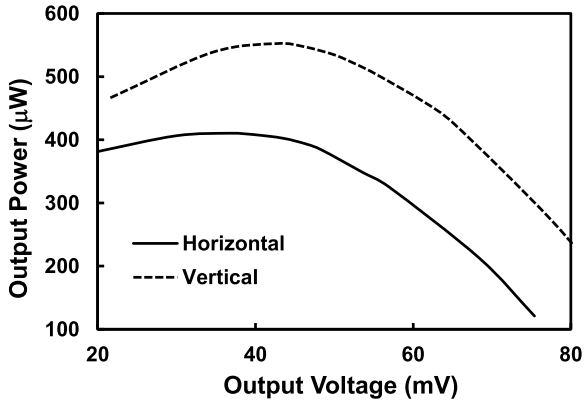

Fig. 6. Output power versus output voltage TEG results for 36.8 °C hot site and 23 °C ambient temperature conditions.

vertical orientations, as shown in Fig. 5, and in still air conditions.

By means of a variable resistor load, the output voltage and the power generated by the TEG have been characterized. The results are shown in Fig. 6 for the output power vs. the output voltage. In horizontal orientation, the maximum output power level is 400 μW with 37-mV output voltage for a measured temperature gradient of 2.5 °C. As observed, a slightly higher output power is obtained when the module is vertically placed. In vertical orientation, the maximum output power is 550 μW with 43-mV output voltage and a measured temperature gradient of 3.5 °C. When compared to the V_L and P_{LMAX} theoretical results of Table I, measured results indicate that the actual internal temperature gradient between the thermocouples has to be lower than the measured temperature gradient between the TEG faces [46]. In fact, a comparison of the measured output voltage levels with the ones shown in Table I indicates that the internal temperature gradient must be around 1.3 °C and 1.5 °C for the horizontal and vertical orientations, respectively. The fact that the optimal

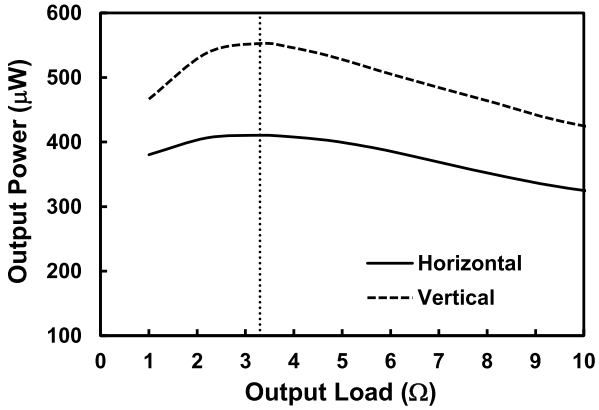

Fig. 7. Output power versus output load TEG results for 36.8 °C hot site and 23 °C ambient temperature conditions.

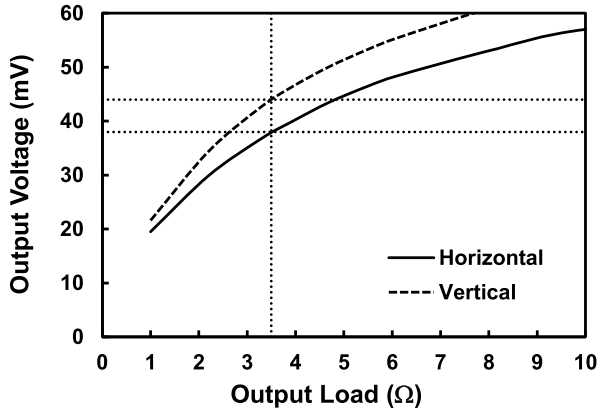

Fig. 8. Output voltage versus output load TEG results for 36.8 °C hot site and 23 °C ambient temperature conditions.

load is 3.3 Ω explains the observed reduction in P_{LMAX}. Still, the resultant output power is enough for the chosen sensor tag application.

In addition, these results also indicate that the optimal load for the TEG is higher than 2.95 Ω. In fact, as shown in Fig. 7, the resistance value that maximizes the output power is 3.3 Ω, which matches the input impedance of the step-up converter (3.5 Ω) so that an output power close to the maximum power is ensured.

Finally, the expected output voltage for the 3.5-Ω input impedance of the step-up converter is shown in Fig. 8. It results in 38 and 44 mV for the horizontal and vertical TEG positions, respectively. Therefore, the TEG is able to provide enough voltage for the up-converter to work at an ambient temperature of 23 °C and a heat source of 36.8 °C.

C. Step-Up Converter Characterization

As previously mentioned, the tag requires a minimum external supply voltage between 1.4 and 3 V in order to work in semi-passive mode. This is much higher than, for example, the 38 mV provided by the TEG when it is horizontally placed. Therefore, a step-up converter is required. The chosen step-up converter uses a 1:100 input transformer in order to up-convert input voltage levels as low as 20 mV to 2.35 V [50].

For its characterization, the up-converter input has been connected to the TEG placed in the horizontal position with the

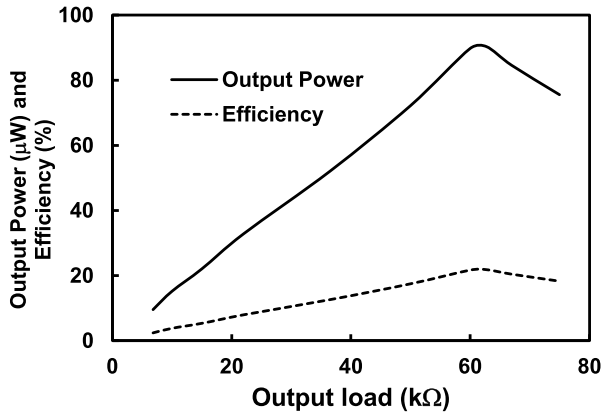

Fig. 9. Output voltage and efficiency versus output load of the set-up converter.

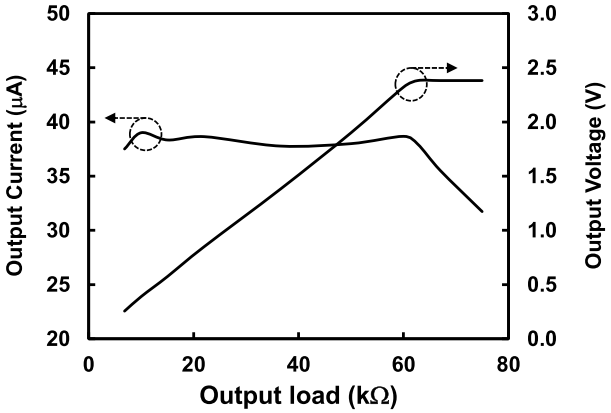

Fig. 10. Output current and output voltage versus output load of the set-up converter.

same previously mentioned temperature conditions. Moreover, the output of the converter is loaded with different resistor values. Test results are shown in Figs. 9 and 10. As observed in Fig. 9, the maximum output power from the step-up converter is 90 μW for 63-KΩ load resistance while reaching a peak efficiency of 22%. In addition, as shown in Fig. 10, the converter is able to provide 40 μA of output current to the load and reaches a constant output voltage up to 2.35 V for the 63 KΩ load and beyond. The measured output power of 90 μW is below the expected output power of 165 μW from Table I. This is due to a higher optimal load of the TEG and a lower measured efficiency for the step-up converter. However, it is almost three times more than the 34.5 μW required by the semi-passive sensor tag. Therefore, the proposed TEG-based energy harvesting system should be able to supply the battery-free sensor tag with only 2.5 °C between hot and cold surfaces of the TEG module.

Finally, if new sensors are added to the system, then higher power is required by the sensor tag. Therefore, the power generated by the TEG needs to be increased. This can be achieved by increasing the TEG size or by connecting several TEG modules in series or parallel. However, a detailed budget analysis is required given that the output voltage and the output resistance of the harvester may change, which consequently modifies the power transfer and the efficiency of the step-up converter.

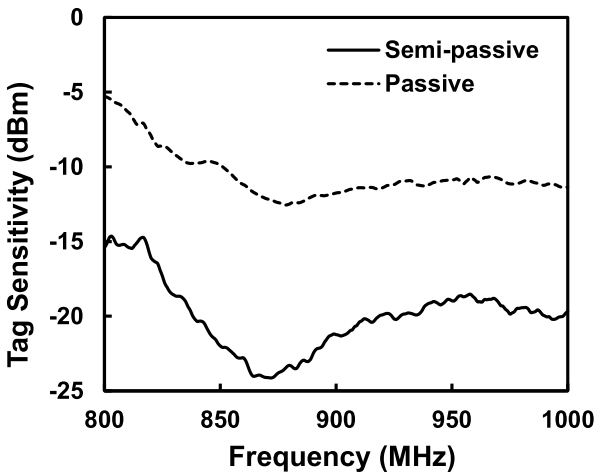

Fig. 11. Sensitivity results of the tag in passive and semi-passive modes measured with the Voyantic Tagformance Pro and query commands.

IV. Test Results

This section details the different tests carried out on the system in order to evaluate the sensor tag in terms of sensitivity and overall communication range in both passive and semi-passive modes.

A. Sensor Tag Sensitivity and Backscatter Efficiency Characterization

The sensor tag has been first characterized both in passive and semi-passive modes with the TagFormance Pro from Voyantic in a laboratory environment. This setup removes the effects of the surrounding environment by calibrating the system with the reference tag that is part of the Voyantic's system [51]. This calibration process is possible because either the sensitivity or the backscattered efficiency of the reference tag is known. During calibration, the UHF band is swept and for each frequency, the reader dynamically adjusts its output power to the minimum value at which the reference tag is able to answer. The difference between the output power of the reader and the sensitivity establishes the forward link losses. In contrast, the backscattered efficiency allows knowing the power backscattered by the reference tag. Thus, the backward link losses can be calculated as the difference between the backscattered power and the power received by the reader.

Once the system has been calibrated, the sensitivity of the tag by checking the answer to an EPC query command has been measured. Test results in Fig. 11 show that the tag sensitivity improves almost 12 dB in semi-passive mode when compared to passive mode, from −12.6 to −24 dBm. These results fit well with the IC-reported performance [44].

The setup also predicts the potential read range of both reader-to-tag (forward) and tag-to-reader (reverse) links. For these read range results, the TagFormance system calculates the forward read range assuming the maximum allowable 2-W ERP in Europe for the transmitted power of the reader. For the reverse read range, the tag's backscattered power is measured and a sensitivity of −74 dBm for the reader is assumed (−70-dBm sensitivity of the reader's front end and 4-dBi gain antenna). The results are shown in Fig. 12. First, as

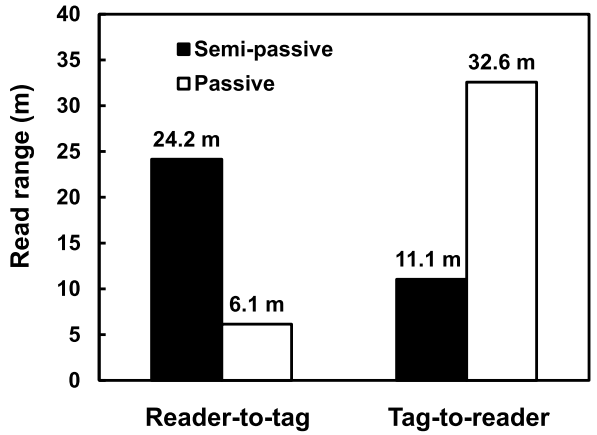

Fig. 12. Forward and reverse read range for the tag in passive and semi-passive modes measured with the Voyantic Tagformance Pro and query commands.

it can be seen, the maximum reader-to-tag read range in the passive mode is limited to 6.1 m, whereas in the semi-passive mode, the forward read range extends to 24.2 m. The semi-passive solution extends the communication range fourfold when compared to the fully passive mode, as expected from the 12-dB difference in sensitivity (free space Friis' formula). Moreover, it is interesting to see how in the passive mode the limiting factor for read range is the tag sensitivity, whereas in the semi-passive mode, the limiting factor is the reader's sensitivity. In fact, a reader with a −74-dBm sensitivity reduces the actual read range to only 11.1 m.

There are different ways to avoid this reverse range limitation. An obvious one is to improve the sensitivity of the reader. However, it is also possible to increase the reverse range by boosting the power backscattered by the tag. In this case, the gain of the tag antenna along with the matching between the antenna and the tag IC plays a significant role [52]. As it is known, RFID tags communicate back to the reader through backscattering. In backscattering, the tag's IC modifies its input impedance, which modulates the incoming wave due to the reflection coefficient change seen by the antenna. The backscatter efficiency quantifies then the proportion of incident wave power that is scattered back from the tag and can be expressed in the following equation:

$$X = K G_{\text{tag}}^2 \tag{9}$$

being G_{tag} the tag's antenna gain and K the modulation loss factor [52]. The modulation loss factor K depends on the tag's antenna and the chip impedance using the following equation:

$$K = \alpha \, |\rho_1 - \rho_2|^2 \tag{10}$$

where α is a modulation-dependent coefficient ($\alpha = 1/4$ for the Gen2 FM0 signaling scheme [53]), and ρ_1 and ρ_2 are the complex reflection coefficients between the antenna impedance (Z_A) and the two different chip loads (Z_1 and Z_2 for the off and active states of the internal modulator) using the following equation:

$$\rho_{1,2} = \frac{Z_{1,2} - Z_A^*}{Z_{1,2} + Z_A^*}. \tag{11}$$

TABLE II
ANTENNA AND TAG IC DIFFERENTIAL IMPEDANCES

Comp/Mode	Frequency (MHz)	Impedance
IC Passive	868	80-j493
IC Semi-passive	868	35-j451
IC Passive	890	71-j485
IC Semi-passive	890	18-j442
IC Passive	915	52-j479
IC Semi-passive	915	14-j456
Dipole Antenna	868	54-j11
Dipole Antenna	890	58+j15
Dipole Antenna	915	63+j36

Normally, antenna-chip matching of passive tags switches from conjugate load ($\rho_1 = 0$) to almost short load ($\rho_2 = -1$), where the latter is achieved by a large capacitor placed in parallel to the RF ports by the internal modulator. Conjugate matching is desired in order to maximize the amount of incident power that is collected by the chip and hence maximize its sensitivity. However, in this case, the modulation loss factor K cannot be higher than −6 dB (assuming $\alpha = 1/4$). Conversely, in semi-passive tags, conjugate matching is not necessarily the optimal solution, because it is the reverse link the limiting factor. In this case, a certain mismatch between the chip and the antenna is preferred in order to increase the backscatter efficiency. Theoretically, K increases up to 0 dB for $\alpha = 1/4$ if the chip input impedances switches between short and open loads. Of course, this is an upper limit because this choice of impedances prevents any RF signal power from being collected by the chip.

With these considerations in mind, in the present design, the effect of the matching network on the backscatter efficiency has been theoretically studied by means of the data in Table II. Specifically, Table II collects the differential impedance values of both the tag chip and the antenna [44]. The latter is a 2-dBi gain dipole antenna that has been designed to cover both the European 868 MHz and the US 915-MHz bands. This antenna presents an S_{11} of −10.8 dB at 868 MHz and an S_{11} of −15.9 dB at 915 MHz. It has an overall length of 137 mm.

As previously mentioned, it is desired that the tag works in both the passive and semi-passive modes. Therefore, by means of an LC differential network shown in Fig. 1 (the series inductors L_{S1} and L_{S2} of 36 nH and the parallel capacitor C_P of 1 pF), the tag IC is conjugate matched to the antenna at 890 MHz in order to cover both 868- and 915-MHz bands in passive mode. However, as seen in Table II, the impedance in the semi-passive mode decreases; consequently, conjugate matching is lost. It is then interesting to anticipate the impact of this matching deviation on the backscatter efficiency using (9)–(11). By means of the values in Table II and assuming a short load when the internal modulator is active, the complex reflection coefficients for both passive and active modes are calculated at 868, 890, and 915 MHz. An example of these calculations is given in Fig. 13 for 868 MHz. The Smith chart shown provides a geometrical interpretation of the $|\rho_1 - \rho_2|$ difference in (10) by considering that the complex reflection

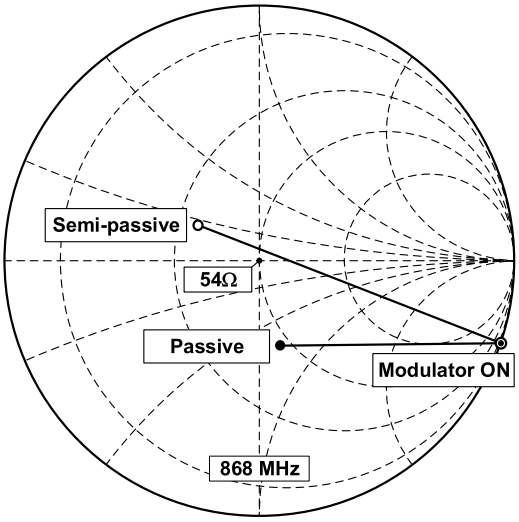

Fig. 13. Graphical representation of the $|\rho 1 - \rho 2|$ difference for tag backscatter efficiency calculation at 868 MHz.

coefficient can be related to a conventional reflection coefficient of a modified load $(Z_L + jX_A)$ (12) [54]:

$$\rho_L = \frac{Z_L - Z_A^*}{Z_L + Z_A^*} = \frac{Z_L + jX_A - R_A}{Z_L + jX_A + R_A} = \rho_{Z_L + jX_A}\big|_{Z_0 = R_A}. \tag{12}$$

As observed, the $|\rho_1 - \rho_2|$ distance in the semi-passive mode is longer than in the passive mode, which indicates higher K and, therefore, better backscattering efficiency in the semi-passive mode. Similar results are obtained at 890 and 915 MHz. As shown in Fig. 14, the improvement in the backscattering efficiency has been both calculated and compared to measurements with the Voyantic TagFormance system. Fig. 14 shows around 3-dB efficiency improvement from passive to semi-passive modes for this tag given the aforementioned matching conditions.

Therefore, with the chosen LC differential network, not only conjugate matching is obtained for maximum power transfer in the passive mode but also an improvement of the backscattering efficiency in the semi-passive mode, which is the bottleneck for the overall read range in this mode case.

B. Reader Solution and Sensor Tag Read Range

A commercial reader module has been chosen in order to test the read range of the sensor tag while sending actual data from the temperature sensor using EPC read commands. The chosen reader is the Nordic ID NUR-05WL2 model. It presents a maximum output power of 27 dBm, which is adjustable in 1-dB steps, a sensitivity of −70 dBm (PER = 0.1%), and a maximum sensitivity of −80 dBm (Listen-Before-Talk). Its power consumption is 2.9 W with dimensions of 106 mm × 72 mm [55]. It has been connected to a 2-dBic (−1 dBi) gain flat antenna. The antenna dimensions are 150 mm × 150 mm [56].

Finally, a Raspberry PI platform is used for the reader control, data logging, and data visualization by means of a user interface. A photograph of the reader prototype and

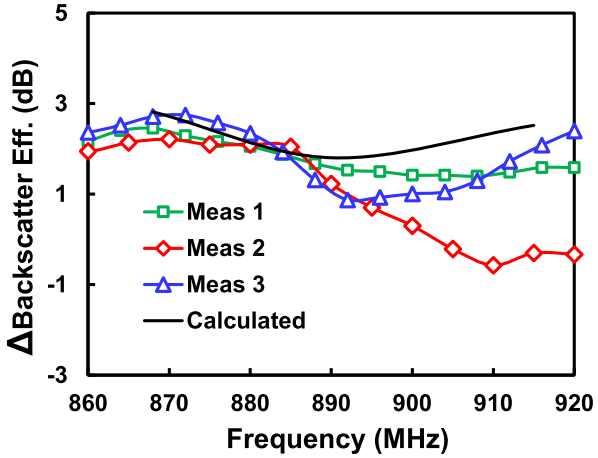

Fig. 14. Theoretical and measured results of the backscatter efficiency improvement of semi-passive mode.

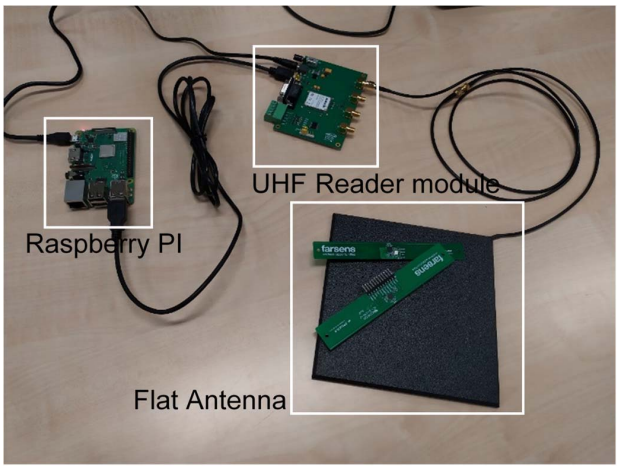

Fig. 15. Photograph of the proposed reader solution.

the developed user interface are shown in Figs. 15 and 16, respectively.

With this system, the forward reading range of the tag was measured both in fully passive and semi-passive modes. The procedure to calculate the forward reading range is as follows.

1) A reference tag with known sensitivity is placed in the measurement setup at a fixed distance from the reader.
2) The output power of the reader is gradually increased until a successful communication is reached.
3) Knowing the reader output power, the reference tag sensitivity, and the wavelength, the path loss is calculated.
4) By comparing the measured path loss with the theoretical loss from the Friis equation, a correction factor is applied to the reader output power. It compensates for the environmental effects.
5) Steps 1 and 2 are repeated with the sensor tag under test using the same measurement set-up although in this case, the control software asks for temperature sensor data by means of read command.
6) Using the reader output power obtained in step 5 and the correction factor of step 4, the tag sensitivity is obtained.
7) Considering the maximum output power of the reader, the communication range is calculated.

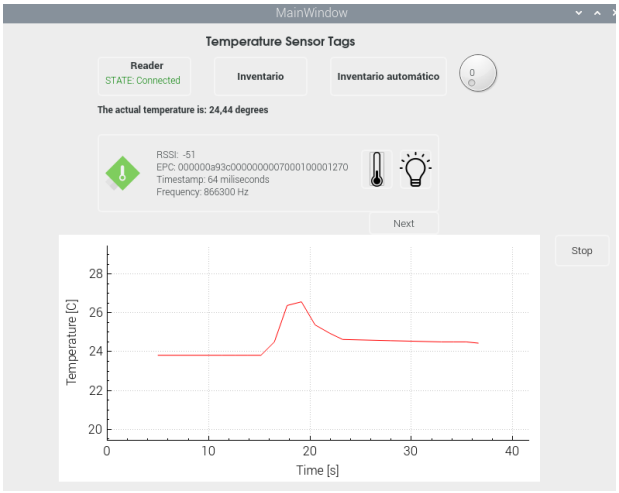

Fig. 16. User interface of the proposed reader solution for temperature reading.

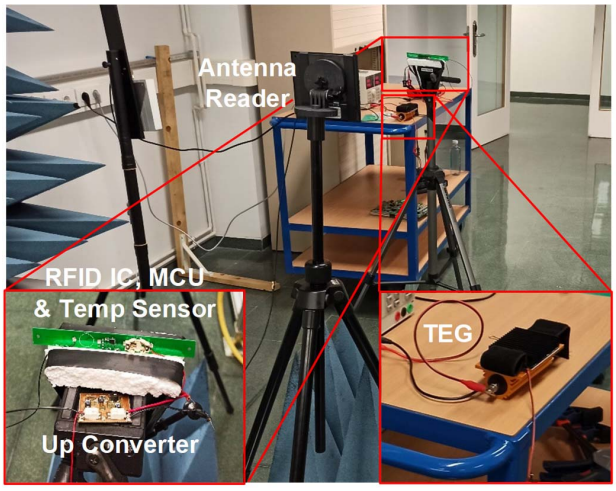

Fig. 17. Photograph of the test setup based on the proposed reader.

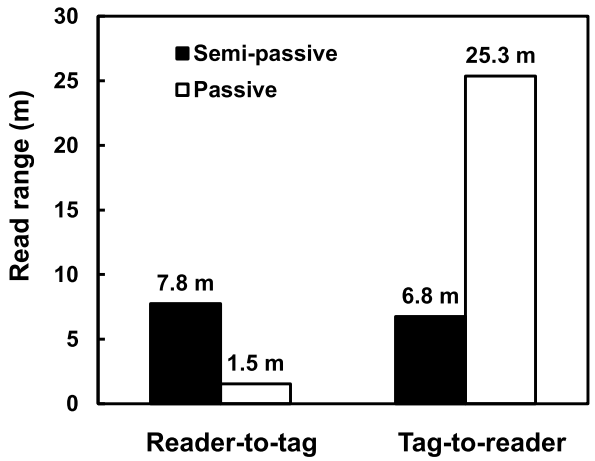

Fig. 18. Tag read range for the passive and semi-passive modes measured with the proposed commercial reader while requesting temperature samples by read commands.

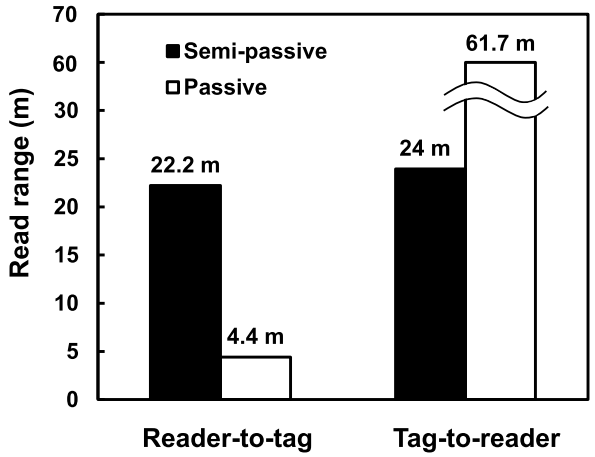

Fig. 19. Tag read range for the passive and semi-passive modes and a 2-W ERP and −80-dBm sensitivity reader while requesting temperature samples by read commands.

A photograph of the setup is shown in Fig. 17. This test procedure has been followed in order to measure the sensitivity of the sensor tag in both its passive and semi-passive modes.

In addition, the reverse read range has been also calculated with the tag sensitivity and path loss measurements obtained from the described procedure, the reader sensitivity, and by means of the backscatter efficiency calculated from Voyantic tests.

Fig. 18 shows the maximum read range results considering the reader capabilities of 26 dBm (27 dBm and −1-dBi antenna gain) maximum output power and a sensitivity of −69 dBm (−70 dBm and −1-dBi antenna gain). For this compact reader-antenna solution, the overall reading range is almost 7 m in the semi-passive mode, limited by the tag-to-reader link. This mode increases five times the read range when compared to the 1.5 m of the passive solution. In fact, tests show that the sensitivity of −24 dBm using EPC query commands is almost preserved when sending temperature samples, with a measured sensitivity of −23 dBm. Conversely, in the passive mode, the sensitivity when sending temperature samples deteriorates to −9 dBm, which is expected due to the increment of power consumption at the sensor tag side [23], [44].

The reading range can be also estimated for the maximum allowable reader output power of 2 W ERP (35.15 dBm) in Europe. As observed in Fig. 19, the reader-to-tag communication range extends to 22.2 m for the semi-passive mode. This read range is four times the read range of the passive mode in this case. As for the tag-to-read communication range, it is 23.7 m for a chosen reader sensitivity of −80 dBm. This value corresponds to the less demanding sensitivity in order to avoid the reverse link being the limiting factor. For the implemented reader solution, with a sensitivity of −70 dBm, this can be achieved with a 10-dBi gain antenna along with a transmitted power of 25.15 dBm.

Finally, the accuracy of the temperature sensor data has also been verified by comparing received temperature samples with a Hanna HI9040 thermistor-based thermometer over the 20 °C–40 °C range with an error well below 1 °C, as expected from the sensor performance.

TABLE III
SoA Comparison

Work	Energy Source	Sensor Types	Sensor Interface	Sensitivity Semi-passive (dBm)	Sensitivity Passive (dBm)	Antenna Gain (dBi)	Range Semi-passive (m)	Range Passive (m)
[22]	RF	Analog	Int. ADC	-15	-7	-	1.13	-
[23]	Photovoltaic	Analog	Built in	-24	-14	2.1	21	3.7
[24]	RF	Analog/Internal	Built-in	-15	-7	8	13*	5.5*
[25]	Photovoltaic	Analog/Internal	Built-in	-15	-7	-	7.3	3.6
[26]	Photovoltaic	Digital/Internal	Built-in	-31	-8	-	7	1
[27]	Photovoltaic	Analog	Custom	-24	-17	4.8	5.4	2.4
[28]	Thermoelectric	Analog/Digital	MCU+SPI	-	-2	2	3	1.75
[29]	Photovoltaic/RF	Analog/Digital	MCU+I2C	-25.3	-18.3	5	27*/7.48*	12.1*/-
[30]	Battery	Digital	MCU+I2C	-25	-	-	17*	-
[31]	Battery	Digital	MCU+SPI	-24.4	-	1.52	13*	-
[32]	Battery	Analog/Digital	MCU+I2C	-24	-17	5	1.5	-
[33]	Battery	Analog/Internal	Built-in	-15	-7	-15	2.8	1
[34]	Battery	Analog	Custom	-27	-18	2	20	-
[35]	Battery	Analog	Built-in	-6.5	-	2	4.3	-
[36]	Battery	Analog/Digital	MCU+SPI	-	-6	2	0.731	-
This work	Thermoelectric	Analog/Digital	MCU+SPI	-24	-12.6	2	22.2	4.4

*Theoretical results based on sensitivity

C. Comparison With the State-of-the-Art

Table III shows the state-of-the-art comparison with recent (last six years) EPC C1G2 compliant semi-passive solutions at the UHF band using both batteries and energy harvesting modules. It is observed that only half of them add a microcontroller to the system in order to allow both digital and analog sensors. The remaining solutions have internal sensors or built-in interfaces for analog sensors, whereas others apply custom sensing techniques. The drawback of these last solutions is that they do not allow for digital sensors that work with SPI or I2C communication protocols, which reduces flexibility for sensor choice. Among the ones including a microcontroller, the proposed solution is the only one with [28] that employs a TEG as the assisting energy source. This work implements a rigid TEG with an area as low as 5.6 cm^2 and uses the same step-up converter. Concerning the harvested power, this work claims a similar output power of 90 μW for similar ambient temperature conditions. However, this system is highly unstable due to the insufficient output voltage provided by the TEG. In fact, this output power value is only possible when there is airflow. In still air conditions, the same conditions used here, and the output power of their solution reduces to 23 μW. Moreover, in a real scenario, the output power they obtain is lower than 11 μW. In fact, the final application is based on a temperature sensor with a maximum read rate of 1 min and an overall power consumption of 4 μW. This is less than the 34.5-μW power consumption and read rate of 4 samples/s of the proposed solution. In addition, the sensor tag of [28] shows a communication range eight times shorter than our proposed sensor tag.

In addition, Table III also shows that the majority of semi-passive solutions employs PV cells as the energy harvesters. Even when a comparison of harvesters using different harvesting mechanisms and energy sources is not straightforward, from the information given in [23], it is possible to compare the performance of a PV harvester with the proposed TEG in terms of power density. The work in [23] characterizes a PV harvester for indoor applications using three samples of a solar cell in series under different lightning sources and intensities. For an overall area of 5.5 cm^2 and choosing a typical indoor light intensity of 800 lux, the module is able to provide 670 μW for a halogen source and 50 μW for a fluorescent or LED source. This corresponds to a 121.4- and 9.1-$\mu W/cm^2$ power density, respectively. The characterized TEG, with an area of 54.4 cm^2, provides 400 μW for a temperature gradient of 2.5 °C (horizontal orientation) and 550 μW for a temperature gradient of 3.5 °C (vertical orientation). This results in a 7.35- and 10.1-$\mu W/cm^2$ power density, respectively. It is observed that TEG power densities are in general lower than the ones offered by PV technology. However, the power density of TEG can match that of PV harvesters depending on the indoor light source.

Finally, the proposed semi-passive solution is the one with the longest communication range while sending data from the sensor. To the best of our knowledge, read range results from [29] (27 m when assisted with a PV cell) are based on tag's sensitivity theoretical calculations and not on actual tests based on sensor data readings.

V. Conclusion

A UHF EPC C1G2/ISO 18000-6C compliant sensor tag has been presented. The sensor tag works both in passive and semi-passive modes. In the semi-passive mode, it includes a flexible TEG, which supplies the energy required to the RFID IC along with a microprocessor and a digital temperature sensor for proper operation. This approach gives extra flexibility to the tag to include new sensors both analog and digital. A power budget analysis has also been performed and demonstrates that the system is able to work even for temperature gradients as low as 2.5 °C resulting from a 36.8 °C hot source, 23 °C ambient temperature, and still air. The sensor tag sensitivity has also been characterized in both passive and semi-passive modes and the maximum read range has been discussed. In addition, a reader prototype has been built in order to test the sensor tag while sending temperature samples with a 2-conv/s resolution. The system demonstrates that the sensor

tag reaches a distance of 22.2 m in the semi-passive mode and 4.4 m in the passive mode while complying with European regulations. Finally, a state-of-the-art comparison shows that the proposed solution is the only one that demonstrates a continuous power source from a flexible TEG and low-temperature gradients. In addition, the presented sensor tag shows the longest read range while sending data from the sensor.

ACKNOWLEDGMENT

The authors would like to thank Ibon Zalbide from Farsens SL for his support and fruitful discussions.

REFERENCES

[1] S. N. R. Kantareddy, I. Mathews, R. Bhattacharyya, I. M. Peters, T. Buonassisi, and S. E. Sarma, "Long range battery-less PV-powered RFID tag sensors," *IEEE Internet Things J.*, vol. 6, no. 4, pp. 6989–6996, Aug. 2019.

[2] P. Mezzanotte, V. Palazzi, F. Alimenti, and L. Roselli, "Innovative RFID sensors for Internet of Things applications," *IEEE J. Microw.*, vol. 1, no. 1, pp. 55–65, Jan. 2021.

[3] I. Farris, S. Pizzi, M. Merenda, A. Molinaro, R. Carotenuto, and A. Iera, "6lo-RFID: A framework for full integration of smart UHF RFID tags into the Internet of Things," *IEEE Netw.*, vol. 31, no. 5, pp. 66–73, Sep. 2017.

[4] M. A. S. Tajin, M. Jacovic, G. Dion, W. M. Mongan, and K. R. Dandekar, "UHF RFID channel emulation testbed for wireless IoT systems," *IEEE Access*, vol. 9, pp. 68523–68534, 2021.

[5] V. Liu, A. Parks, V. Talla, S. Gollakota, D. Wetherall, and J. R. Smith, "Ambient backscatter: Wireless communication out of thin air," in *Proc. ACM SIGCOMM Conf. (SIGCOMM)*, Aug. 2013, pp. 1–13.

[6] J. Kimionis, A. Bletsas, and J. N. Sahalos, "Increased range bistatic scatter radio," *IEEE Trans. Commun.*, vol. 62, no. 3, pp. 1091–1104, Mar. 2014.

[7] S. Megalou, A. G. Dimitriou, A. Tzitzis, and T. V. Yioultsis, "Design and fabrication of a compact, low-cost UHF-RFID repeater, exploiting circular cross-polarization," *IEEE J. Radio Freq. Identificat.*, vol. 5, no. 1, pp. 64–74, Mar. 2021.

[8] S. Chen, S. Zhong, S. Yang, and X. Wang, "A multiantenna RFID reader with blind adaptive beamforming," *IEEE Internet Things J.*, vol. 3, no. 6, pp. 986–996, Dec. 2016.

[9] A. DiNatale, A. DiCarlofelice, and E. DiGiampaolo, "A crack mouth opening displacement gauge made with passive UHF RFID technology," *IEEE Sensors J.*, vol. 22, no. 1, pp. 174–181, Jan. 2022.

[10] M. Wagih and J. Shi, "Wireless ice detection and monitoring using flexible UHF RFID tags," *IEEE Sensors J.*, vol. 21, no. 17, pp. 18715–18724, Sep. 2021.

[11] K. Bouzaffour, B. Lescop, P. Talbot, F. Gallee, and S. Rioual, "Development of an embedded UHF-RFID corrosion sensor for monitoring corrosion of steel in concrete," *IEEE Sensors J.*, vol. 21, no. 10, pp. 12306–12312, May 2021.

[12] M. A. S. Tajin, C. E. Amanatides, G. Dion, and K. R. Dandekar, "Passive UHF RFID-based knitted wearable compression sensor," *IEEE Internet Things J.*, vol. 8, no. 17, pp. 13763–13773, Sep. 2021.

[13] C. Huang, B. Huang, B. Zhang, Y. Li, J. Zhang, and K. Wang, "An electromagnetically induced transparency inspired antenna sensor for crack monitoring," *IEEE Sensors J.*, vol. 21, no. 1, pp. 651–658, Jan. 2021.

[14] M. A. S. Tajin, W. M. Mongan, and K. R. Dandekar, "Passive RFID-based diaper moisture sensor," *IEEE Sensors J.*, vol. 21, no. 2, pp. 1665–1674, Jan. 2021.

[15] Q. H. Dang, S. J. Chen, D. C. Ranasinghe, and C. Fumeaux, "Modular integration of a passive RFID sensor with wearable textile antennas for patient monitoring," *IEEE Trans. Compon., Packag., Manuf. Technol.*, vol. 10, no. 12, pp. 1979–1988, Dec. 2020.

[16] D. Inserra *et al.*, "Screw relaxing detection with UHF RFID tag," *IEEE Access*, vol. 8, pp. 78553–78564, 2020.

[17] N. Khalid, R. Mirzavand, H. Saghlatoon, M. M. Honari, and P. Mousavi, "A three-port zero-power RFID sensor architecture for IoT applications," *IEEE Access*, vol. 8, pp. 66888–66897, 2020.

[18] X. Chen *et al.*, "Passive moisture sensor based on conductive and water-soluble yarns," *IEEE Sensors J.*, vol. 20, no. 18, pp. 10989–10995, Sep. 2020.

[19] Y. Shafiq, J. Henricks, C. P. Ambulo, T. H. Ware, and S. V. Georgakopoulos, "A passive RFID temperature sensing antenna with liquid crystal elastomer switching," *IEEE Access*, vol. 8, pp. 24443–24456, 2020.

[20] P. Sen, S. N. R. Kantareddy, R. Bhattacharyya, S. E. Sarma, and J. E. Siegel, "Low-cost diaper wetness detection using hydrogel-based RFID tags," *IEEE Sensors J.*, vol. 20, no. 6, pp. 3293–3302, Mar. 2020.

[21] I. Ullah, R. Horne, B. Sanz-Izquierdo, and J. C. Batchelor, "RFID AC current sensing technique," *IEEE Sensors J.*, vol. 20, no. 4, pp. 2197–2204, Feb. 2020.

[22] A. Rigi, A. Mugisha, A. Arefian, S. R. Khan, and S. Mitra, "Wireless battery-free body temperature sensing device for key workers," *IEEE Sensors Lett.*, vol. 6, no. 2, pp. 1–4, Feb. 2022.

[23] A. Astigarraga *et al.*, "A 21 m operation range RFID tag for 'Pick to light' applications with a photovoltaic harvester," *Micromachines*, vol. 11, no. 11, p. 1013, Nov. 2020.

[24] S. Ma, N. Pournoori, L. Sydanheimo, L. Ukkonen, T. Bjorninen, and A. Georgiadis, "A batteryless semi-passive RFID sensor platform," in *Proc. IEEE Int. Conf. RFID Technol. Appl. (RFID-TA)*, Sep. 2019, pp. 171–173.

[25] A. Abdelnour, A. Hallet, S. B. Dkhil, P. Pierron, D. Kaddour, and S. Tedjini, "Energy harvesting based on printed organic photovoltaic cells for RFID applications," in *Proc. IEEE Int. Conf. RFID Technol. Appl. (RFID-TA)*, Sep. 2019, pp. 110–112.

[26] S. N. R. Kantareddy, I. Mathews, R. Bhattacharyya, I. M. Peters, T. Buonassisi, and S. E. Sarma, "Long range battery-less PV-powered RFID tag sensors," *IEEE Internet Things J.*, vol. 6, no. 4, pp. 6989–6996, Aug. 2019.

[27] A. E. Abdulhadi and T. A. Denidni, "Self-powered multi-port UHF RFID tag-based-sensor," *IEEE J. Radio Freq. Identificat.*, vol. 1, no. 2, pp. 115–123, Jun. 2017.

[28] I. Jauregi *et al.*, "UHF RFID temperature sensor assisted with body-heat dissipation energy harvesting," *IEEE Sensors J.*, vol. 17, no. 5, pp. 1471–1478, Mar. 2017.

[29] A. E. Abdulhadi and R. Abhari, "Multiport UHF RFID-tag antenna for enhanced energy harvesting of self-powered wireless sensors," *IEEE Trans. Ind. Informat.*, vol. 12, no. 2, pp. 801–808, Apr. 2016.

[30] R. Colella *et al.*, "Design and technology transfer of RFID-based medical sensing devices," in *Proc. IEEE Int. Conf. RFID Technol. Appl. (RFID-TA)*, Oct. 2021, pp. 191–194.

[31] R. Colella *et al.*, "Design of UHF RFID sensor-tags for the biomechanical analysis of human body movements," *IEEE Sensors J.*, vol. 21, no. 13, pp. 14090–14098, Jul. 2021.

[32] D. Jayawardana, R. Liyanapathirana, and X. Zhu, "RFID-based wireless multi-sensory system for simultaneous dynamic acceleration and strain measurements of civil infrastructure," *IEEE Sensors J.*, vol. 19, no. 24, pp. 12389–12397, Dec. 2019.

[33] C. Miozzi, S. Nappi, S. Amendola, C. Occhiuzzi, and G. Marrocco, "A general-purpose configurable RFID epidermal board with a two-way discrete impedance tuning," *IEEE Antennas Wireless Propag. Lett.*, vol. 18, no. 4, pp. 684–687, Apr. 2019.

[34] E. DiGiampaolo, A. DiCarlofelice, and A. Gregori, "An RFID-enabled wireless strain gauge sensor for static and dynamic structural monitoring," *IEEE Sensors J.*, vol. 17, no. 2, pp. 286–294, Jan. 2017.

[35] V.-H. Duong, N. X. Hieu, H.-S. Lee, and J.-W. Lee, "A battery-assisted passive EPC Gen-2 RFID sensor tag IC with efficient battery power management and RF energy harvesting," *IEEE Trans. Ind. Electron.*, vol. 63, no. 11, pp. 7112–7123, Nov. 2016.

[36] M. Tanaka, N. Takahashi, R. Ikeda, H. Yoda, and M. Suzuki, "Development and evaluation of a ground coil monitoring system using semi-passive sensor tags," in *Proc. IEEE Int. Conf. RFID Technol. Appl. (RFID-TA)*, Sep. 2015, pp. 141–146.

[37] M. Markiewicz *et al.*, "Software controlled low cost thermoelectric energy harvester for ultra-low power wireless sensor nodes," *IEEE Access*, vol. 8, pp. 38920–38930, 2020.

[38] I. Mathews, S. N. Kantareddy, T. Buonassisi, and I. M. Peters, "Technology and market perspective for indoor photovoltaic cells," *Joule*, vol. 3, no. 6, pp. 1415–1426, 2019.

[39] V. Pecunia, L. G. Occhipinti, and R. L. Z. Hoye, "Emerging indoor photovoltaic technologies for sustainable Internet of Things," *Adv. Energy Mater.*, vol. 11, no. 29, pp. 1–31, Aug. 2021.

[40] N. Jaziri, A. Boughamoura, J. Müller, B. Mezghani, F. Tounsi, and M. Ismail, "A comprehensive review of thermoelectric generators: Technologies and common applications," *Energy Rep.*, vol. 6, pp. 264–287, Dec. 2020.
[41] Perpetua Power Source Technologies, Inc., Use Cases. (2021). *Thermoelectric Delivers Power for All Industries*. Accessed: Jun. 16, 2022. [Online]. Available: https://perpetuapower.com/use-cases/
[42] ABB, Application Description AG/CP101-EN. (2012). *Temperature Measurement in Steam Pipes of Chemical Plants*. Accessed: Jun. 16, 2022. [Online]. Available: https://library.e.abb.com/public/401f386cb606afb8c12579ad00444586/AG_CP101-EN_02-2012.pdf
[43] (2019). *Farsens SL, Industrial Application Uses*. Accessed: Jun. 16, 2022. [Online]. Available: http://www.farsens.com/en/applications/industrial/
[44] *Farsens SL, ROCKY100 IC Data Sheet*. Accessed: Jun. 16, 2022. [Online]. Available: http://www.farsens.com/wp-content/uploads/2017/12/DS-ROCKY100-V04.pdf
[45] *Texas Instruments, TMP112 Digital Temperature Sensor*. Accessed: Jun. 16, 2022. [Online]. Available: https://www.ti.com/product/TMP112
[46] A. Proto *et al.*, "A flexible thermoelectric generator Worn on the leg to harvest body heat energy and to recognize motor activities: A preliminary study," *IEEE Access*, vol. 9, pp. 20878–20892, 2021.
[47] C. S. Kim *et al.*, "Structural design of a flexible thermoelectric power generator for wearable applications," *Appl. Energy*, vol. 214, pp. 131–138, Mar. 2018.
[48] *Tegway, Flexible Thermoelectric Device*. Accessed: Jun. 16, 2022. [Online]. Available: http://tegway.co/tegway/
[49] *Arctic, MX-4 High Performance Thermal Paste*. Accessed: Jun. 16, 2022. [Online]. Available: https://www.arctic.de/media/69/a5/63/1632839894/Spec_Sheet_MX-4_EN.pdf
[50] (2019). *Analog Devices, LTC3108 Ultralow Voltage Step-Up Converter and Power Manager*. Accessed: Jun. 16, 2022. [Online]. Available: https://www.analog.com/media/en/technical-documentation/data-sheets/LTC3108.pdf
[51] (2022). *Tagformance Pro Protocol Analyzer RAIN RFID and NFC Testing and Measurement Systems for Research & Development*. Accessed: Jun. 16, 2022. [Omline]. Available: https://voyantic.com/lab/tagformance-pro/
[52] P. V. Nikitin and K. V. S. Rao, "LabVIEW-based UHF RFID tag test and measurement system," *IEEE Trans. Ind. Electron.*, vol. 56, no. 7, pp. 2374–2381, Jul. 2009.
[53] P. V. Nikitin and K. V. S. Rao, "Antennas and propagation in UHF RFID systems," in *Proc. IEEE Int. Conf. (RFID)*, Apr. 2008, pp. 277–288.
[54] J. C. Bolomey, S. Capdevila, L. Jofre, and J. Romeu, "Electromagnetic modeling of RFID-modulated scattering mechanism. Application to tag performance evaluation," *Proc. IEEE*, vol. 98, no. 9, pp. 1555–1569, Sep. 2010.
[55] *Nordic ID, NUR Innovation Board*. Accessed: Jun. 16, 2022. [Online]. Available: https://www.nordicid.com/wp-content/uploads/nordic-id-nur-05wl2-rfid-module_datasheet_eu_v1006.pdf
[56] *Nordic ID, FA1515e Flat Antenna*. Accessed: Jun. 16, 2022. [Online]. Available: https://www.nordicid.com/wp-content/uploads/Nordic-ID-FA1515e-Antenna_Datasheet_V1001.pdf

Hector Solar received the M.Sc. degree in telecommunication engineering from the University of Pais Vasco, Bilbao, Spain, in 2002, and the Ph.D. degree in electronic engineering from Tecnun-School of Engineering, Technological Campus, University of Navarra, Donostia-San Sebastian, Spain, in 2007.

In 2007, he was a Researcher with the Electronics and Communications Division, CEIT, Donostia-San Sebastian. Through CEIT, he has collaborated in the design RF/mm-wave, low-power sensors, and RFID devices in CMOS. He has been an External Consultant of Seiko–Epson, Barcelona, Spain, from 2006 to 2007. He is currently an Associate Professor with the Department of Electrical and Electronic Engineering, Tecnun—University of Navarra. He has authored or coauthored more than 40 international journal and conference papers. He holds one patent. He coauthored two books: *Linear CMOS RF Power Amplifiers: A Complete Design Workflow* (Springer, 2014) and *Systems Design for Remote Healthcare* (Springer, 2014). His research interests include CMOS RF/mm-wave integrated circuit design and low-power analog circuit design with a special emphasis on batteryless sensor nodes.

Andoni Beriain (Member, IEEE) received the M.Sc. and Ph.D. degrees in telecommunication engineering from Tecnun—University of Navarra, Donostia-San Sebastian, Spain, in 2008 and 2013, respectively, with a focus on low-power sensor interface design.

From 2013 to 2018, he was devoted to the design of the analog front-end and mixed-signal blocks of a sensor enabled passive RFID chip marketed as Rocky100 by Farsens Company. He is currently an Associate Professor with the Department of Electrical and Electronic Engineering, Tecnun—University of Navarra. His current research interests include long-range RFID sensor applications and energy harvesters and power management units for autonomous sensor nodes.

Ainhoa Rezola received the M.Sc. and Ph.D. degrees in telecommunication engineering from the Tecnun—University of Navarra, Donostia-San Sebastian, Spain, in 2013 and 2017, respectively.

She joined the Department of Electronic and Communication, CEIT Research Center, Donostia-San Sebastian, in 2013. In 2019, she was a Visiting Postdoctoral Researcher with the Department of Electrical and Computer Engineering, University of California at Santa Barbara (UCSB), Santa Barbara, CA, USA. She is currently an Associate Professor with the Department of Electrical and Electronic Engineering, Tecnun—University of Navarra. She has published numerous articles in national and international conferences, as well as in specialized journals. She is also the author of a technical book and an international patent. Since 2013, her research has focused on the design of digital systems, especially on the design and implementation of hardware platforms based on microprocessor and FPGA.

David del Rio (Member, IEEE) received the M.Sc. and Ph.D. degrees in telecommunication engineering from the Tecnun—University of Navarra, Donostia-San Sebastian, Spain, in 2013 and 2017, respectively, with a focus on BiCMOS transmitters for multi-Gbps *E*-band communications.

In 2016, he was a Visiting Graduate Researcher with the High Speed Electronics Laboratory, University of California at Los Angeles, Los Angeles, CA, USA, where he was involved in the design of CMOS integrated transceivers for 5G communications. He is currently a Researcher with the Electronics Systems and Communications Group, CEIT Research Center, Donostia-San Sebastian. He is also an Associate Professor with the Department of Electrical and Electronic Engineering, Tecnun—University of Navarra. His current research interests include millimeter-wave (mmW) and RF circuit design, power amplifiers, phased arrays, and reconfigurable devices for self-healing systems.

Roc Berenguer (Senior Member, IEEE) received the M.Sc. and Ph.D. degrees from Tecnun, Technological Campus, University of Navarra, Donostia-San Sebastian, Spain, in 1996 and 2000, respectively.

From 1999 to 2015, he was with CEIT, Donostia-San Sebastian, Spain. Through CEIT and INCIDE (spin-off of the CEIT's COMMIC Group), he worked as an External Consultant with Siemens, Munich, Germany in 2000; Hitachi Microsystems Europe, Maidenhead, U.K., 2001; Xignal Technologies, Munich, Germany, from 2001 to 2002; Seiko-Epson, Barcelona, Spain, from 2006 to 2007; and Innophase, San Diego, CA, USA, from 2012 to 2022, where he collaborated in the design of several RF front ends for wireless standards like GSM-EDGE, DAB, and Wibree. He is currently an Associate Professor with the Department of Electrical and Electronic Engineering, Tecnun—University of Navarra. He is the author or coauthor of more than 70 refereed publications in journals and conferences. He holds ten patents and is the coauthor of the books: *Design and Test of High Quality Integrated Inductors for RF Applications in Conventional Technologies* (Springer, 2003), *GPS and Galileo: Dual RF Front-End Receiver Design*, *Fabrication, and Test* (McGraw-Hill, 2008), and *Linear CMOS RF Power Amplifiers: A Complete Design Workflow* (Springer, 2014). His technical expertise and research interests are in the areas of CMOS RF/mm-wave IC design, ultralow-power analog circuit design for battery-less sensor nodes, and high-speed signal processing.

Dr. Berenguer is an Assessor of the Spanish Agency of Evaluation and Prospective (ANEP). He served for the TPC of the IEEE European Solid State Circuit Conference, IEEE Midwest Symposium Circuits and Systems, and the IEEE Ph.D. Research in Microelectronics and Electronics. He also served as a Reviewer for several journals, such as IEEE JOURNAL OF SOLID-STATE CIRCUITS, IEEE TRANSACTIONS ON MICROWAVE THEORY AND TECHNIQUES, IEEE TRANSACTIONS ON CIRCUITS AND SYSTEMS—I: REGULAR PAPERS, and IEEE TRANSACTIONS ON CIRCUITS AND SYSTEMS—II: EXPRESS BRIEFS.